arXiv:1408.4374v3 [cond-mat.str-el] 18 Jul 2015

Resonating valence-bond physics on the honeycomb lattice

Pranay Patil,[1] Ishita Dasgupta,[2] and Kedar Damle[3]

[1]*Dept. of Physics, Indian Institute of Technology Madras, Chennai 600036*
[2]*Dept. of Physics, Indian Institute of Technology Bombay, Mumbai 400076*
[3]*Dept. of Theoretical Physics, Tata Institute of Fundamental Research, Mumbai 400005*

We study bond and spin correlations of the nearest-neighbour resonating valence bond (RVB) wavefunction for a SU(2) symmetric $S = 1/2$ antiferromagnet on the honeycomb lattice. We find that spin correlations in this wavefunction are short-ranged, while the bond energy correlation function takes on an oscillatory power-law form $D(\vec{r}) \sim \cos(\mathbf{Q}\cdot\vec{r})/|\vec{r}|^{\eta_w(2)}$, where $\mathbf{Q} = (2\pi/3, -2\pi/3)$ is the wavevector corresponding to "columnar" valence-bond solid order on the honeycomb lattice, and $\eta_w(2) \approx 1.49(3)$. We use a recently introduced large-g expansion approach to relate bond-energy correlators of the SU(g) wavefunction to dimer correlations of an interacting fully-packed dimer model with a three-dimer interaction of strength $V(g) = -\log(1 + 1/g^2)$. Putting $g = 2$, we find numerically that the dimer correlation function $D^d(\vec{r})$ of this dimer model has power-law behaviour $D^d(\vec{r}) \sim \cos(\mathbf{Q}\cdot\vec{r})/|\vec{r}|^{\eta_d(2)}$ with $\eta_d(2) \approx 1.520(15)$, in rather good agreement with the wavefunction results. We also study the same quantities for $g = 3, 4, 10$ and find that the bond-energy correlations in the SU(g) wavefunction are consistently well-reproduced by the corresponding dimer correlations in the interacting dimer model.

I. INTRODUCTION

As is well-known, localized electronic moments (spins) in Mott-insulating materials typically interact with near-neighbours via antiferromagnetic exchange interactions which can be much bigger than the weak magnetic dipole interactions between these localized moments. The possibility that such quantum antiferromagnets remain in a liquid-like phase down to the lowest temperature has attracted sustained interest since the early work of Fazekas and Anderson[1].

This has motivated the study of candidate wavefunctions that describe various quantum spin liquid ground states. Here, our focus is on a particular construction that works directly in the overcomplete basis of singlet (valence) bonds between spins, by specifying amplitudes for various ways in which the spins can pair up to make singlets. The full "resonating valence bond" (RVB) wavefunction is then a superposition of all these possibilities, with these amplitudes chosen by some physically motivated rule. On bipartite lattices, it is possible to choose the phase of these amplitudes so as to satisfy the Marshall sign-rule[2], which is known to be obeyed in the ground state of a large class of antiferromagnets. Indeed, in their original study of such RVB wavefunctions on the square lattice, Liang, Doucot and Anderson[3] had fixed the sign-structure in this manner to study the variational energy of the square-lattice $S = 1/2$ Heisenberg antiferromagnet as a function of the length distribution of valence bonds. They concluded that the short-ranged RVB wavefunction with valence-bonds allowed only between pairs of nearest-neighbour spins gives a variational energy that is only slightly higher than that of a trial Néel ordered state, which has long-ranged valence-bonds in this basis.

More recent work has built on these results in several ways: First, Tang, Sandvik and Henley[4] and Albuquerque and Alet[5] revisited the square lattice nearest-neighbour RVB (nnRVB) wavefunction using the loop algorithm of Sandvik and Evertz[6] to sample expectation values in the nnRVB wavefunction. They found that bond-energy correlations have a slow, oscillatory power-law decay. This is in complete contrast to the extremely short-ranged spin correlations in this wavefunction. Second, Cano and Fendley[7] constructed a spin Hamiltonian with short-ranged couplings whose ground state is the nnRVB wavefunction on the square lattice. Third, one of the present authors, in collaboration with Dhar and Ramola, developed a cluster-expansion approach that relates the bond-energy correlations in this square lattice wavefunction to dimer correlations of a specific interacting dimer model, whose leading interaction is an attraction between pairs of parallel dimers on adjacent bonds of the square lattice[8]. Some aspects of this correspondence were also checked by Stéphan *et. al.*[9] in their study of the entanglement properties of this wavefunction. In the three-dimensional case, Albuquerque, Alet and Moessner[10] showed that the nnRVB wavefunction on the cubic and diamond lattices has long-range antiferromagnetic order, underlining the importance of dimensionality in determining the nature of correlations in this kind of variational wavefunction. Additionally, recent work by Xu and Beach[11] suggests that an anisotropic version of the three-dimensional nnRVB wavefunction describes interesting spin-liquid behaviour.

In the present study, we focus on extending these results to antiferromagnets on the honeycomb lattice. Our primary motivation is to test the correspondence between bond-energy correlations in the nnRVB wavefunction and dimer correlations of a fully-packed dimer model with certain interactions, the form of which we derive here using the methods of Ref. 8. To this end, we study both sides of this correspondence using Monte-Carlo simulations. Our computational results rely heavily on a new update-scheme[12] that allows a more efficient and ergodic Monte-Carlo sampling of valence-bond configurations when used in conjunction with the Sandvik-Evertz

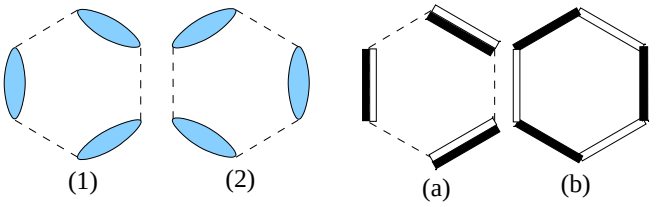

FIG. 1: (1) and (2) represent the two flippable configurations of dimers around a hexagon (here dimers are represented by ellipses). The weight of configuration (1) in the interacting dimer model gets contributions from the two loop configurations (a) and (b) of the loop model equivalent to the nnRVB wavefunction. This is captured by the effective interactions between dimers worked out in the text.

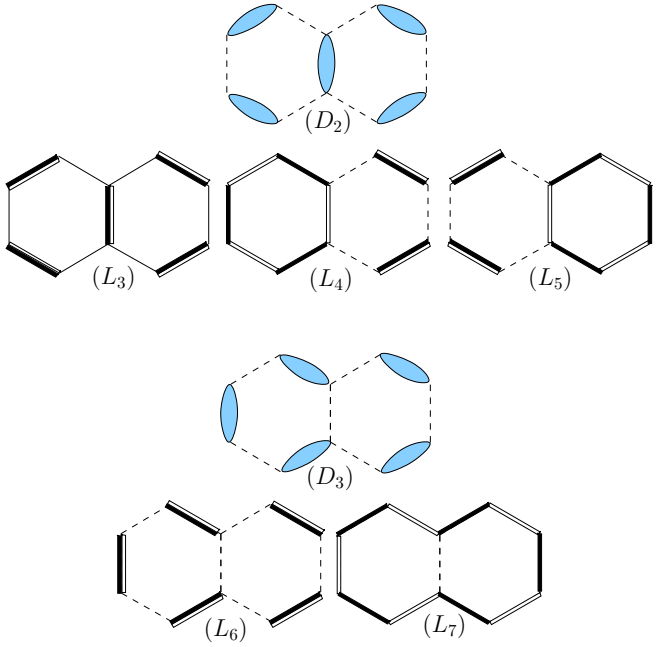

FIG. 2: D_2 shows a configuration with two flippable hexagons that share a dimer. The weight for such a configuration in the interacting dimer model gets contributions from loop configurations L_3, L_4, and L_5. Similarly, D_3 represents one of the two flippable arrangements of dimers around on the perimeter of a double-hexagon. The weight for such a configuration in the interacting dimer model gets contributions from loop configurations L_6, L_7, and L_4.

algorithm[6]. To place both our wavefunction and dimer model results in the context of a long-wavelength height-model description[17–27], we first provide a self-contained account of the correspondence between the height-model stiffness and power-law exponents for dimer and bond-energy correlators, and derive the form of the dependence of the reduced dimer partition function on winding numbers. Although both these results are available in earlier literature[24–27], our formulation of the latter may be of some independent interest since it makes explicit the three-fold symmetry of the honeycomb lattice.

The rest of this article is organized as follows: In Section II we establish the correspondence between the nnRVB wavefunction on the honeycomb lattice and an interacting fully-packed dimer model on the same lattice, with a specific form of the interactions, which we derive. In Section III, we discuss the coarse-grained height-model description of fully-packed dimers on the honeycomb lattice, paying particular attention to features that are specific to the honeycomb lattice case. We derive the dependence of the restricted partition function on winding number sectors, and summarize the correspondence between height-model stiffness and various power-law exponents. We also indicate how this can be carried over to our wavefunction studies. In Section IV, we summarize a new update-scheme[12] for Monte-Carlo sampling of valence-bond configurations, and explain how it improves the ergodicity of our simulations when used in conjunction with the well-known Sandvik-Evertz algorithm[6]. In Section V, we describe our numerical results on the nnRVB wavefunction for SU(g) antiferromagnets (with $g = 2, 3, 4, 10$) and the corresponding interacting dimer model, and demonstrate that the dimer correlations in the latter provides a rather good account of the bond-energy correlations in the former. We close with a brief discussion of our results in Section VI.

II. VALENCE-BONDS AND FULLY-PACKED INTERACTING DIMERS

The nearest neighbour RVB wavefunction for a bipartite SU(2) antiferromagnet with $S = 1/2$ spins at each site is given by a uniform amplitude superposition of all possible SU(2) valence bond solid states in which each spin makes a singlet with one of its neighbours. This construction generalizes readily to the SU(g) case when the SU(g) spins on one sublattice carry the fundamental representation and those on the other sublattice carry the complex conjugate of the fundamental. In general, we write

$$|\psi(g)\rangle = \sum_D |D\rangle_g \tag{1}$$

where

$$|D\rangle_g = \prod_{l\in D} |\phi_o(g)\rangle_l \tag{2}$$

where D is any complete dimer cover of the bipartite lattice, l denotes all links covered by dimers of D, $|\phi_o(g)\rangle_l$ is the SU(g) singlet state of the two spins connected by l, and A and B denote the A and B sublattice sites connected by link l. The norm is given by:

$$\langle\psi(g)|\psi(g)\rangle = \sum_{D,D'} \langle D|D'\rangle_g \tag{3}$$

which can be written as the partition function of a fully packed loop model with non-intersecting loops[13–16]. To see this, one notes that a superposition of two fully-packed dimer-covers gives a fully-packed configuration of loops. Thus, we identify the inner product of $|D\rangle$ and $|D'\rangle$ with the loop configuration L whose weight $w_{loop}(g, L)$ is determined by the quantum-mechanical overlap between these two singlet states. The norm of the wavefunction can thus be written as the loop gas partition function

$$Z_{loop}(g) = \sum_{L} w_{loop}(g, L). \tag{4}$$

Here, $w_{loop}(g, L) = (g)^{n_d(L)}(2g)^{n_l(L)}$, where $n_d(L)$ is the number of trivial length-two loops (doubled-edges) in the loop configuration L (corresponding to bra and ket valence bonds occupying the same link) and $n_l(L)$ is the number of non-trivial (length-four or more) loops in L. Operator expectation values in this wavefunction, such as spin correlation and bond-energy correlation functions, are obtained from Monte-Carlo estimators defined entirely in terms of this loop gas[13–16]. For instance, in the SU(2) case, the two-point correlation function of spins is simply three-fourth of the probability that both spins lie on the same overlap loop. The estimator for the two-point function of the bond-energy operator $\vec{S}_i \cdot \vec{S}_j$ corresponding to a nearest-neighbour bond $\langle ij \rangle$, *i.e.* the correlation of bond-energies at $\langle ij \rangle$ and $\langle kl \rangle$, is only slightly more complicated: It involves the probabilities for various ways in which the four points i, j, k, l lie on at most two loops of the loop gas[13–16]. Both these results have natural generalizations[13–16] to the SU(g) case.

As was noted in earlier work[8], if the loop gas is in a short-loop phase, corresponding to exponentially decaying spin correlations in the RVB wavefunction, there is a precise mapping between the loop gas and an interacting fully-packed dimer model defined on the same bipartite lattice. This mapping is perturbative in g^{-1}, and leads to a dimer model with n-dimer interactions whose strength decays rapidly with n when g is large. Under this mapping, bond-energy correlators in the RVB wavefunction map to dimer correlators in this interacting dimer model, apart from an overall prefactor[8]. In the square-lattice case, this mapping has proved to be a useful way to understand the power-law bond-energy correlations in the SU(2) wavefunction[8].

Here, we use this approach[8] to derive the form of this interacting dimer model for the honeycomb lattice case. Following Ref. 8, the n-dimer interaction is given recursively by the following relation :

$$-\log[w_{dimer}(g, D_n)] = V_n(D_n) + \sum_{m=1}^{n-1} \sum_{D_m \epsilon D_n} V_m(D_m), \tag{5}$$

where

$$w_{dimer}(g, D_n) = \sum_{L|D_n} \frac{w_{loop}(g, L)}{2^{n_l(L)}}, \tag{6}$$

where $L|D_n$ denotes all possible loop configurations that contribute to the weight of a given n-dimer configuration D_n, and $D_m \epsilon D_n$ denotes all sub-configurations of this n-dimer configuration. Using the above relation, we see that the one-body potential (fugacity) goes as $-\log(g)$. This simply says that each dimer contributes a factor of g to the dimer model partition function; since we are considering a fully-packed dimer model, this just fixes the overall normalization of the partition function. From this recursion relation, we also see that every two-body term is zero. The only three-body term lives on a flippable hexagon (dimer configurations labeled (1) and (2) in Fig 1), which has two possible loop configurations that contribute to the weight of each such flippable dimer configuration; for instance, loop configurations labeled a and b contribute to the dimer configuration labeled (1) in Fig 1 (and similarly for (2)). Thus, flippable hexagons are favoured in the interacting dimer model by an attractive three-body term:

$$V_3(g) = -\log(1 + g^{-2}). \tag{7}$$

Using these results, it is easy to see that the four-body potential is zero. There are two five-dimer configurations which have a non-zero interaction energy (Fig 2). The first, labeled D_2 in Fig. 2, gets contributions from loop configurations L_3, L_4, and L_5 as shown in Fig. 2. The second, labeled D_3, gets contributions from loop configurations L_4, L_6 and L_7. Thus, we have the two five-body interaction potentials

$$V_5^a(g) = -\log(1 - (g^2 + 1)^{-2}), \tag{8}$$

$$V_5^b(g) = -\log(1 + (g^4 + g^2)^{-1}). \tag{9}$$

From this recursive analysis, it is easy to see that n-body terms, when non-zero, are generally of order $O(g^{-(n-1)})$ for $n > 2$. In our computations we only use the leading order non-trivial interaction (which is the three-body term). As we will see in later sections, this already gives a rather good account of the bond-energy correlators in the SU(g) wavefunction for $g = 2, 3, 4, 10$.

III. HEIGHT MODEL

In this section, we lay the groundwork to place both our wavefunction and dimer model results in the context of a long-wavelength height-model description[17–27]. To this end, we provide a self-contained account of the correspondence between the height-model stiffness and power-law exponents for dimer and bond-energy correlators, and derive the form of the dependence of the reduced partition function on winding numbers. Although both these results are available in earlier literature[24–27], our formulation of the latter may be of some independent interest since it makes explicit the three-fold symmetry of the honeycomb lattice.

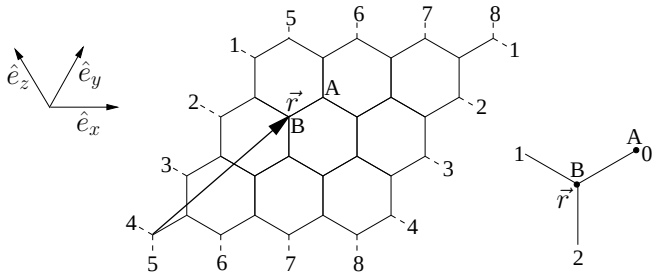

FIG. 3: The honeycomb lattice is constructed using a two point basis of sites A and B "belonging" to each Bravais lattice point $\vec{r} = m\hat{e}_x + n\hat{e}_y$ with integer m and n, which, in our convention, is the coordinate of the B-sublattice site. When talking of bond-energies or dimer occupation numbers, we use the convention that three types of bonds 0, 1, and 2 "belong" to each $\vec{r}$, as shown in the figure.

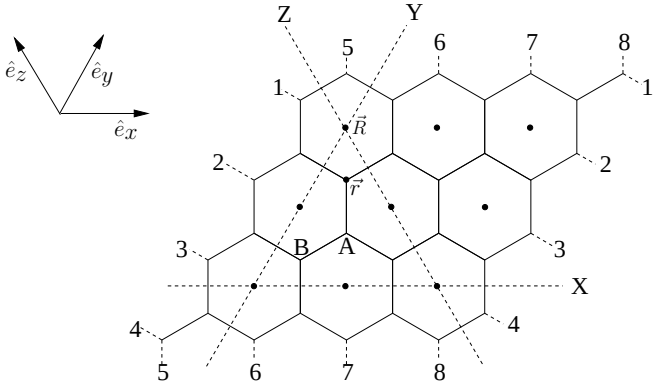

FIG. 4: B-sublattice honeycomb sites are labeled by $\vec{r}$ and their corresponding triangular lattice counterparts are labeled $\vec{R}$. Also shown here are the lines across which dimer or valence-bond flux is calculated to get three winding numbers w_x, w_y and w_z as described in the text.

We begin by defining a microscopic height field $H(\vec{R})$ on the triangular lattice dual to the honeycomb lattice (Fig. 3 and Fig. 4) in the following manner: Given a configuration of dimers on the honeycomb lattice, and fixing the height at the origin of the triangular lattice to be $H(\vec{O}) = 0$, we construct $H(\vec{R})$ on sites $\vec{R}$ of the dual triangular lattice using the rules give below

$$H(X+1,Y) - H(X,Y) = n_2(x,y+1) - \frac{1}{3}\ , \qquad (10)$$

$$H(X,Y+1) - H(X,Y) = -n_1(x,y+1) + \frac{1}{3}\ , \qquad (11)$$

$$H(X-1,Y+1) - H(X,Y) = n_0(x-1,y+1) - \frac{1}{3}\ , \qquad (12)$$

where $n_\mu(\vec{r})$ is 1 if the $\mu^{\rm th}$ type bond belonging to point $\vec{r}$ (Fig. 3) is occupied by a dimer and 0 otherwise. Here, $\vec{r} = (x,y)$ is the coordinate of a B-sublattice site of the honeycomb lattice, we assign the same coordinate to the A-sublattice site "belonging" to $\vec{r}$ (as shown in Fig. 3), and $\vec{R} = (X,Y)$ is the coordinate of the corresponding dual triangular lattice site that coincides with the center of the hexagon vertically above this B-sublattice site. Clearly, this microscopic height H is uniquely defined for all fully-packed configurations, and takes on one-third-integer values.

As is well-understood[17–27], a fully-packed dimer configuration, and "nearby" configurations accessible to it via local rearrangements, all correspond to the same coarse-grained height-field. Dimer states with many such nearby configurations give rise to a coarse-grained height-field with small tilt. If the dimer model is in a power-law ordered state, one expects that long-wavelength fluctuations of the height-field will be determined by this entropic cost of tilting the height configuration, while the restriction that H takes on values that are one-third of an integer is expected to be irrelevant as far as long-distance properties are concerned. One therefore postulates that long-wavelength properties of such fully-packed dimer models are captured by a coarse-grained *real-valued* height field h whose statistics is governed by a Gaussian action[17–27] $S_{\rm renorm.} \sim (\nabla h)^2$, *i.e* a statistical weight proportional to $\exp(-\text{const.}\int d^2r(\nabla h)^2)$.

Here, we prefer a hybrid approach whereby we work with a *real-valued* height field $h(\vec{R})$ that is defined on the dual triangular lattice sites $\vec{R}$. This is equivalent to re-discretizing the coarse-grained height action on the dual triangular lattice, instead of imposing an isotropic cutoff in momentum-space. Thus, we postulate that a height configuration $h(\vec{R})$ has statistical weight $\exp(-S)$, where S has the form

$$S = \pi\kappa_d \sum_{\langle \vec{R}\vec{R}'\rangle} (h_{\vec{R}} - h_{\vec{R}'})^2 \qquad (13)$$

where the sum is over all nearest neighbour bonds $\langle \vec{R}\vec{R}'\rangle$ of the triangular lattice, and κ_d is a phenomenological stiffness constant.

As is well-known[24], long-distance properties of correlations of $n_\mu(\vec{r})$ ($\mu = 0,1,2$) are well-described in this language by an operator correspondence made up of two parts. One part, in the vicinity of the uniform wavevector $\vec{q} = 0$, is given by lattice-gradients of $\vec{h}(\vec{R})$, and follows directly from the construction of the microscopic heights outlined earlier, while the other part[24] encodes physics in the vicinity of wavevector $\vec{q} = \mathbf{Q} \equiv (\frac{2\pi}{3}, -\frac{2\pi}{3})$, which is the wavevector corresponding to columnar ordering in the honeycomb dimer model. More explicitly, we have:

$$n_0(\vec{r}) = \frac{1}{3} + \Delta_z h + c\mathrm{Re}(e^{i\mathbf{Q}\cdot\vec{r}} e^{2\pi i \overline{h}_0(\vec{r})})\ , \qquad (14)$$

$$n_1(\vec{r}) = \frac{1}{3} - \Delta_y h + c\mathrm{Re}(e^{i\mathbf{Q}\cdot\vec{r} + \frac{2\pi i}{3}} e^{2\pi i \overline{h}_1(\vec{r})})\ , \qquad (15)$$

$$n_2(\vec{r}) = \frac{1}{3} + \Delta_x h + c\mathrm{Re}(e^{i\mathbf{Q}\cdot\vec{r} + \frac{4\pi i}{3}} e^{2\pi i \overline{h}_2(\vec{r})})\ , \qquad (16)$$

where c is a phenomenological constant, $\Delta_\mu h$ denotes the lattice-gradient in the positive μ direction ($\mu = 0, 1, 2$) along the link of the dual triangular lattice which cuts across the honeycomb lattice bond labeled $(\vec{r}, \mu)$ (Fig. 3 and Fig. 4), and $\overline{h}_\alpha(\vec{r})$ ($\alpha = A, B$) denotes the average of $h(\vec{R})$ over the three triangular lattice points surrounding the honeycomb lattice point labeled by α and $\vec{r}$.

In our simulations, we study the nnRVB wavefunction and the corresponding interacting dimer model on $L \times L$ lattices with periodicity of L lattice units in the $\hat{e}_x$ and $\hat{e}_y$ directions. On such periodic lattices, fully-packed dimer configurations may be labeled by three winding numbers satisfying one constraint. The winding numbers are defined in terms of the number of dimers N_x, N_y, and N_z that are encountered as we follow the dotted lines X, Y and Z around the torus (Fig. 4). The definition is simply $w_\mu = N_\mu - L/3$ ($\mu = x, y, z$). Clearly $w_x + w_y + w_z = 0$ in any fully-packed configuration, since the total number of dimers of all orientations equals L^2 and N_μ are independent of where we cut the lattice to count these integers (both these statements are a straightforward consequence of the fully-packed nature of each configuration).

For L a multiple of 3 (as is always the case in our numerics), w_μ are integers. For the coarse-grained height field used in our analytical effective field-theory calculations, these integers define twisted boundary conditions, whereby $h(\vec{R})$ changes by an amount equal to w_μ upon winding around the torus in the positive μ direction. In a coarse-grained sense, this corresponds to a constant gradient of strength w_μ/L in the μ direction. Therefore, the relative statistical weight of winding sector (w_x, w_y, w_z) of the honeycomb dimer model is expected to be proportional to

$$\exp(-\pi\kappa_d({w_x}^2 + {w_y}^2 + {w_z}^2)) \tag{17}$$

Thus, simply measuring the relative frequency of different winding sectors in a Monte-Carlo simulation gives a direct handle on the phenomenological stiffness parameter κ_d. This is one of three ways in which we extract κ_d in our simulations. As we now discuss, the other two ways have to do with dimer correlations at wavevectors $\vec{q} = \mathbf{Q}$ and $\vec{q}$ in the vicinity of 0.

For wavevectors near $\vec{q} = 0$, if we measure solely in the zero-winding sector (corresponding to periodic boundary conditions on h), we expect

$$N_0(\vec{q}) = \langle n_0(\vec{q}) n_0(-\vec{q}) \rangle_{0c} = \frac{1}{2\pi\kappa_d} \left(\frac{(q_x - q_y)^2}{{q_x}^2 + {q_y}^2 + (q_x - q_y)^2} \right) \tag{18}$$

$$N_1(\vec{q}) = \langle n_0(\vec{q}) n_0(-\vec{q}) \rangle_{0c} = \frac{1}{2\pi\kappa_d} \left(\frac{(q_y)^2}{{q_x}^2 + {q_y}^2 + (q_x - q_y)^2} \right) \tag{19}$$

and

$$N_2(\vec{q}) = \langle n_0(\vec{q}) n_0(-\vec{q}) \rangle_{0c} = \frac{1}{2\pi\kappa_d} \left(\frac{(q_x)^2}{{q_x}^2 + {q_y}^2 + (q_x - q_y)^2} \right) \tag{20}$$

in the limit $|\vec{q}| \to 0$. Here, the subscript indicates that we take only the connected part of this correlation function and measure only in the zero-winding sector, and we have used the convention $\vec{q} = (q_x, q_y) \equiv q_x \hat{l}_x + q_y \hat{l}_y$ where $\hat{l}_x$ and $\hat{l}_y$ are reciprocal lattice vectors satisfying $\hat{l}_x \cdot \hat{e}_x = \hat{l}_y \cdot \hat{e}_y = 1$ and $\hat{l}_x \cdot \hat{e}_y = \hat{l}_y \cdot \hat{e}_x = 0$. Each of the N_μ approach a limiting value of $1/(4\pi\kappa_d)$ when $\vec{q}$ is taken to zero along two directions each: Thus, N_0 approaches this value when $\vec{q} = (q, 0)$ or $\vec{q} = (0, q)$, N_1 approaches this value when $\vec{q} = (q, q)$ or $\vec{q} = (0, q)$, and N_2 approaches this value when $\vec{q} = (q, q)$ or $\vec{q} = (q, 0)$. This suggests that we may estimate κ_d rather accurately from $N(|\vec{q}|)$, the average of these six limits.

On the other hand, the connected correlation function of $n_\mu(\vec{r})$ at large spatial separation is dominated by the physics at wavevector $\vec{q} = \mathbf{Q}$. For instance, from the operator correspondence displayed earlier, we expect

$$\langle n_0(\vec{r}) n_0(0,0) \rangle_c \sim \cos(\mathbf{Q} \cdot \vec{r}) \langle e^{2\pi i \overline{h}_0(\vec{r})} e^{-2\pi i \overline{h}_0(0)} \rangle \ . \tag{21}$$

Evaluating the expectation value on the right-hand-side using the effective action S, we find

$$\langle n_0(\vec{r}) n_0(0,0) \rangle \sim \frac{\cos(\mathbf{Q} \cdot \vec{r})}{r^{\eta_d}} \ , \tag{22}$$

where

$$\eta_d \ = \ \frac{\mathcal{C}}{2\pi\kappa_d} \ , \tag{23}$$

with

$$\mathcal{C} = \int_0^{2\pi} \frac{d\theta}{2 + \sin 2\theta} = \frac{2\pi}{\sqrt{3}} \ .$$

In other words, we expect correlators at wavevector $\mathbf{Q}$ to decay as a power-law, with power-law exponent $\eta_d = 1/(\kappa_d\sqrt{3})$; this reflects the power-law valence-bond solid (VBS) order present in the system. We therefore expect that a measurement of such power-law correlators at large spatial separations provides a third independent way of extracting κ_d.

Turning to the nnRVB wavefunction, we note that the valence-bonds in the bra define one fully-packed dimer configuration while the valence-bonds in the ket define another fully-packed dimer configuration. The results of Ref. 8 imply that these two dimer configurations have exponentially small probability for being in two different winding sectors for large L. This is expected to be true whenever the wavefunction represents a genuine spin-liquid, or, equivalently, whenever all overlap loops are small. Since this is the case in our wavefunction study, we restrict attention to the sub-class of loop-model configurations in which there is no net winding of the loops. In this restricted ensemble, which we study numerically when we sample the nnRVB wavefunction, the definition of winding sectors given for the dimer model goes over unchanged: We simply keep track of the common winding numbers w_μ of the bra/ket valence-bond configuration.

This allows us to obtain an effective κ_w for the wavefunction directly from the analog of Eqn. 17, by simply keeping track of the histogram of these winding numbers.

From the analysis of Ref. 8, we also expect that the connected bond-energy correlator $D(\vec{r}) = \langle P_{\langle ij \rangle} P_{\langle kl \rangle} \rangle_c$ where $\vec{r}$ is the separtion between bonds $\langle ij \rangle$ and $\langle kl \rangle$ and $P_{\langle ij \rangle}$ is the singlet projector on bond $\langle ij \rangle$, has the same long-distance behaviour as the connected dimer correlation of dimers living on these two bonds. Therefore, by measuring this quantity and fitting to an oscillatory power-law decay $\cos(\mathbf{Q} \cdot \vec{r})/r^{\eta_w(g)}$, we can extract a power-law exponent $\eta_w(g)$ for the wavefunction, and thence, an effective stiffness parameter $\kappa_w(g) = 1/(\eta_w(g)\sqrt{3})$ exactly as in Eqn. 22 and Eqn. 23 in the dimer case.

Finally, we may form the average $\bar{n}_\mu(\vec{r})$ ($\mu = 0, 1, 2$) of the valence-bond occupation variables in the bra and the ket configuration, and consider the connected correlation functions of $\bar{n}_\mu(\vec{r})$ near wavevector $\vec{q} = 0$. From the results of Ref. 8, we expect these to have behaviour exactly analogous to that displayed in Eqn. 18, Eqn. 19, and Eqn. 20 for the dimer model. By measuring $N(|\vec{q}|)$, the average of the six different small $|\vec{q}|$ limits defined earlier, we expect to obtain a third independent estimate of the effective stiffness parameter $\kappa_w(g)$ for the SU(g) wavefunction. These prescriptions for extracting an effective stiffness $\kappa_w(g)$ from our wavefunction simulations are in direct correspondence with similar ideas used in Ref. 4 in the square-lattice case.

IV. ALGORITHM

Our simulations of the interacting dimer model use the well-known dimer worm algorithm of Ref. 27. This allows us to straightforwardly obtain high-precision results for various dimer correlation functions even at large L. Our wavefunction simulations are however much more challenging, and require some new algorithmic developments.

In order to appreciate the algorithmic difficulties involved, it is useful to start with the following key observation, which forms the basis of the analysis in Ref. 8: When overlap loops between bra and ket valence-bonds are on average rather small, as is the case in the spin-liquid phase, we may think of the corresponding loop-gas in terms of a picture consisting of densely-packed short loops. In the $g \to \infty$ limit where all loops are the shortest possible, *i.e.* doubled-edges, we may thus caricature the system by thinking in terms of a fully-packed dimer model where the dimers now correspond to doubled edges.

If this large-g caricature of the system provides a good approximation to long-distance properties of correlations in the nnRVB wavefunction, bra and ket valence-bonds must necessarily be tied to each other quite strongly. This has important implications for the efficiency of the standard Sandvik-Evertz algorithm[6]. To see this, we recall that this algorithm, when applied to wavefunction studies, consists of two steps: In the first step, one updates the bra (ket) valence-bond configuration using a dimer worm algorithm[27], while keeping the ket (bra) configuration and the auxillary spin-states[6] fixed. In the second step, one updates the spin-states along randomly chosen overlap loops.

When one performs a dimer worm update[27] on either the bra valence-bond configuration or the ket valence-bond configuration, the worm construction has to respect the constraints provided by the background auxillary spin-configuration, which remains static. As a result, most worms grown by the dimer worm algorithm are extremely small, and it is impossible to change the bra or the ket valence-bond configuration except very slowly. This leads to serious equilibriation problems that affect the accuracy of measurements of bond-energy correlations and winding sector probabilities in the nnRVB wavefunction simulations for large L and g[12].

The solution[12] to these algorithmic difficulties suggests itself immediately if one thinks in terms of this large-g caricature for the short-loop phase: Motivated by this caricature, one introduces an additional update scheme, whereby a worm algorithm is used to simultaneously move the bra and ket valence-bonds that comprise doubled-edges in the loop representation. In other words, one considers the sub-system made up of bra and ket valence-bonds that cover the same link of the honeycomb lattice, *i.e.* the part of the lattice which is covered by doubled-edges. This subsystem is updated using a standard worm algorithm[27] applied to the doubled-edges. In doing so, other valence-bonds, that form part of non-trivial overlap loops of length greater than two, are held fixed. The spin configuration on sites visited by such non-trivial loops is also held fixed. However, the spin labels on sites touched by doubled-edges are updated during the construction of the worm using the following prescription: If the worm construction starts with a A (B) sublattice site, spin-states of all B (A) sublattice sites encountered in the worm construction are left unchanged, while spin-states of all A (B)sublattice sites encountered in the worm construction are made consistent with the spin-state of the B (A) sublattice site to which they are connected by a doubled-edge in the final valence-bond configuration (after the worm has updated that part of the lattice).

This additional update scheme greatly improves the ergodicity of our simulations. We have tested it thoroughly in the present case and confirmed that results on small systems are identical to those obtained using the conventional Sandvik-Evertz algorithm. At large sizes and large g, this additional update provides us a way of obtaining accurate results for bond-energy correlations, and for the relative weight of different winding number sectors. This improvement is key to obtaining reliable results for the larger values of g we study.

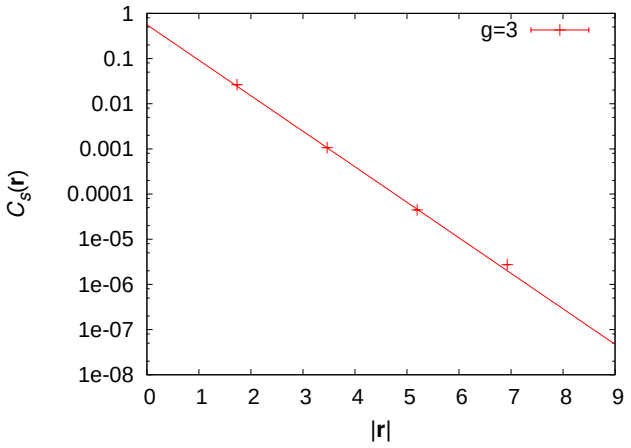

FIG. 5: Spin correlation function between two sites on the same sublattice, separated by $\vec{r}$. The fit is to an exponentially decaying function $c\exp(-r/\xi)$, with best-fit value of correlation length $\xi = 0.550(14)$.

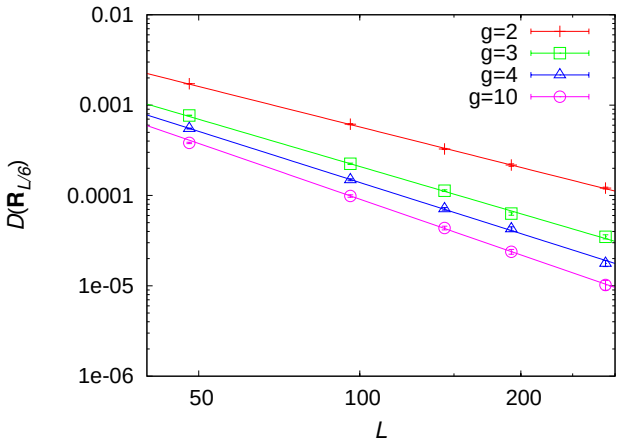

FIG. 6: $D(\vec{R}_{L/6})$ as a function of L for $g = 2, 3, 4$ and 10. $\eta_w(g)$ extracted from a fit to the form $cL^{-\eta_w(g)}$ gives $\eta_w(2) = 1.49(3)$, $\eta_w(3) = 1.74(6)$, $\eta_w(4) = 1.88(5)$, and $\eta_w(10) = 2.04(7)$. $\eta_w(g)$ is expected to equal $1/(\kappa_w(g)\sqrt{3})$, providing us a way of estimating $\kappa_w(g)$.

V. NUMERICAL STUDIES

In our wavefunction studies, we study $L \times L$ systems of $2L^2$ spins(Fig 3), where L a multiple of 12 ranging from $L = 48$ to $L = 288$. To characterize the Néel order in the ground state, it is conventional to construct the corresponding order parameter

$$\vec{M}_s = \frac{1}{L^2}\sum_{\vec{r}} \vec{m}(\vec{r}) \tag{24}$$

where $\vec{m}$ is the local Néel order parameter field defined as

$$\vec{m}(\vec{r}) = \vec{S}_{\vec{r}A} - \vec{S}_{\vec{r}B} \tag{25}$$

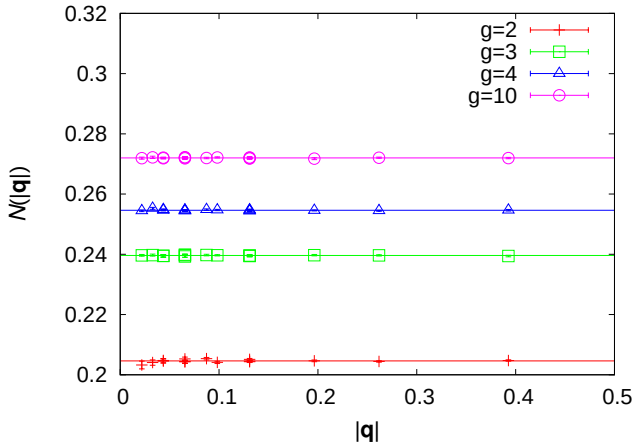

FIG. 7: $N(\vec{q})$ is the correlator of the average valence-bond occupation variables (defined in Sec. III) in the limit of small $|\vec{q}|$, measured in the zero-winding sector (defined in Sec. III) of our wavefunction simulations. The extrapolation to $|\vec{q}| \to 0$ yields intercepts of 0.2046(2), 0.2396(2), 0.2546(3) and 0.2722(2) for $g = 2, 3, 4$ and 10 respectively. These intercepts are expected to equal $1/(4\pi\kappa_w)$, and provide us an accurate estimate of $\kappa_w(g)$.

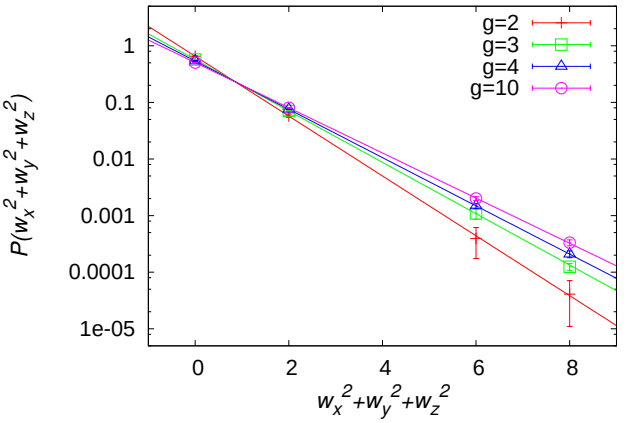

FIG. 8: Winding sector probabilities for the nnRVB simulation at $g = 2, 3, 4$ and 10, plotted as a function of $w^2 \equiv w_x^2 + w_y^2 + w_z^2$. The fit is to an exponentially decaying function $a\exp(-c(g)w^2)$, with best-fit values $c(2) = 1.218(5)$, $c(3) = 1.045(1)$, $c(4) = 0.982(3)$, and $c(10) = 0.919(3)$. $c(g)$ is expected to equal $\pi\kappa_w(g)$, providing a means of estimating $\kappa_w(g)$.

where $\vec{r}A$ ($\vec{r}B$) refers to the A (B) sublattice site "belonging" to Bravais lattice site $\vec{r}$ (Fig. 3). We have studied the L dependence of $\langle \vec{M}_s^2 \rangle$ in the SU(g) wavefunction and confirmed that there is no long-range Néel order for any g. The short-ranged nature of spin correlations are particularly obvious in our results for the spin correlation

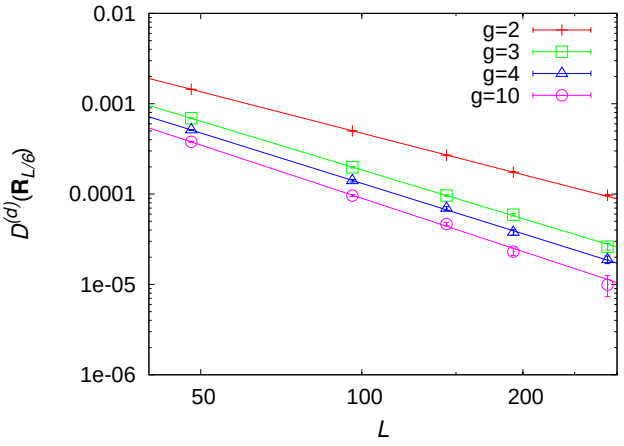

FIG. 9: $D^{(d)}(\vec{R}_{L/6})$ as a function of L for $g = 2, 3, 4$ and 10. $\eta_d(g)$ extracted from a fit to the form $cL^{-\eta_d(g)}$ gives $\eta_d(2) = 1.520(15)$, $\eta_d(3) = 1.79(2)$, $\eta_d(4) = 1.85(4)$ and $\eta_d(10) = 1.96(9)$. $\eta_d(g)$ is expected to equal $1/(\kappa_d(g)\sqrt{3})$, providing us a way of estimating $\kappa_d(g)$.

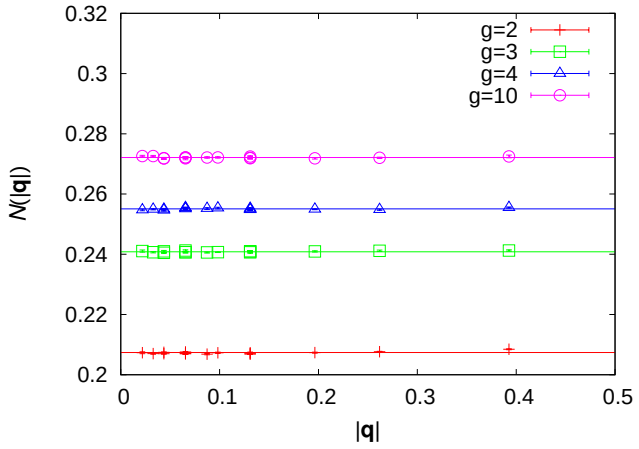

FIG. 10: $N(\vec{q})$ is the correlator of the average dimer correlation function (defined in Sec. III) in the limit of small $|\vec{q}|$, measured in the zero-winding sector (defined in Sec. III) of our dimer-model simulations. The extrapolation to $|\vec{q}| \to 0$ yields intercepts of 0.2074(1), 0.2408(1), 0.2551(1) and 0.2721(1) for $g = 2, 3, 4$ and 10 respectively. These intercepts are expected to equal $1/(4\pi\kappa_d)$, and provide us an accurate estimate of $\kappa_d(g)$.

function:

$$C_s(\vec{r}) = \frac{\mathcal{A}_g}{L^2} \sum_{\vec{r}'} \langle \vec{S}_A(\vec{r}' + \vec{r}) \cdot \vec{S}_A(\vec{r}') \rangle \qquad (26)$$

Here, $\vec{S}$ are spin-half operators in the $g = 2$ case; more generally, they are spin $S = (g-1)/2$ operators in the SU(g) case. The normalization $\mathcal{A}_g = 3/(g^2-1)$ is inserted to yield a Monte-Carlo estimator[13–16] that takes on a g-independent value for a given configuration of loops.

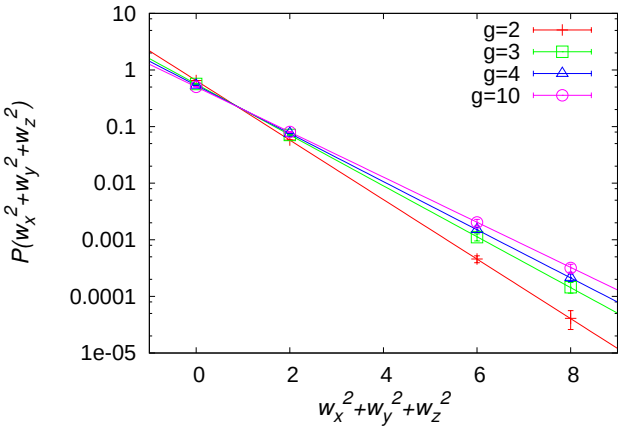

FIG. 11: Winding sector probabilities for the dimer-model simulation at $g = 2, 3, 4$ and 10, plotted as a function of $w^2 \equiv w_x^2 + w_y^2 + w_z^2$. The fit is to an exponentially decaying function $a \exp(-c(g)w^2)$, with best-fit values $c(2) = 1.211(4)$, $c(3) = 1.036(4)$, $c(4) = 0.979(4)$, and $c(10) = 0.918(3)$. $c(g)$ is expected to equal $\pi\kappa_d(g)$, providing a means of estimating $\kappa_d(g)$.

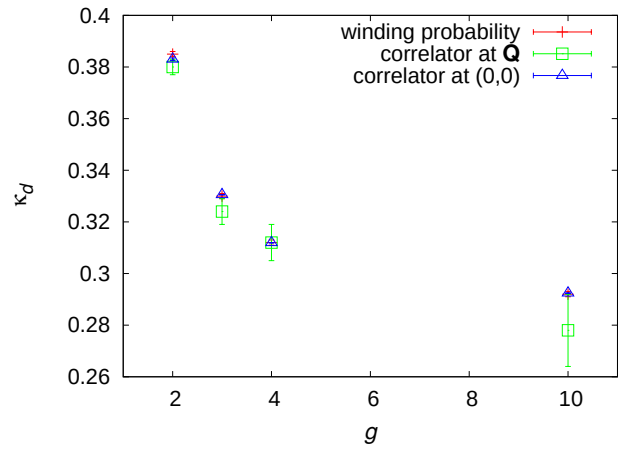

FIG. 12: Comparisons of values of κ_d obtained using different methods for $g = 2, 3, 4$ and 10.

To characterize the tendency towards power-law VBS order at the columnar wavevector $\mathbf{Q}$, we define the columnar VBS order parameter $\Psi = \sum_{\vec{r}} V_{\vec{r}}$, where $V_{\vec{r}}$ is the local VBS order parameter field defined as:

$$V_{\vec{r}} = (P_{\vec{r}0} + e^{2\pi i/3} P_{\vec{r}1} + e^{4\pi i/3} P_{\vec{r}2}) e^{i\vec{Q}\cdot\vec{r}} \, . \qquad (27)$$

Here $P_{\vec{r}\mu}$ ($\mu = 0, 1, 2$) denotes the SU(g) singlet projector on the bond labeled by μ and $\vec{r}$ (Fig. 3), and $\mathbf{Q} \equiv (2\pi/3, -2\pi/3)$ (Fig. 3). In our numerical work, we find it convenient to compute correlations of $V_{\vec{r}}$

$$D(\vec{R}_{\alpha L}) = \frac{\mathcal{B}_g}{L^2} \sum_{\vec{r}} \langle V^\dagger_{\vec{r}+\vec{R}} V_{\vec{r}} + V^\dagger_{\vec{r}} V_{\vec{r}+\vec{R}} \rangle \qquad (28)$$

at separations $\vec{R}_{\alpha L} = (\alpha L, \alpha L)$ with $\alpha = \frac{1}{3}, \frac{1}{4}, \frac{1}{6}$. Here,

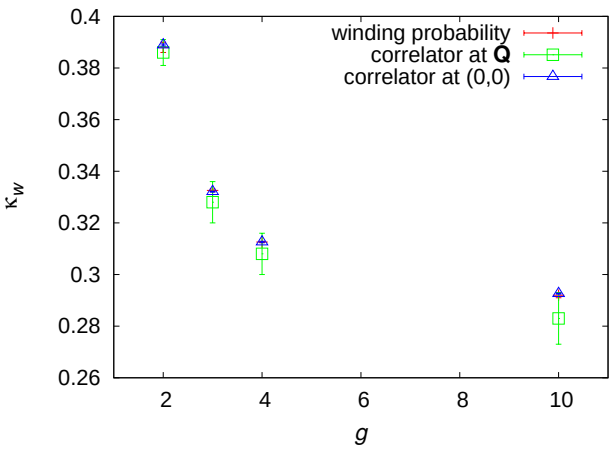

FIG. 13: Comparisons of values of κ_w obtained using different methods for $g = 2, 3, 4$ and 10.

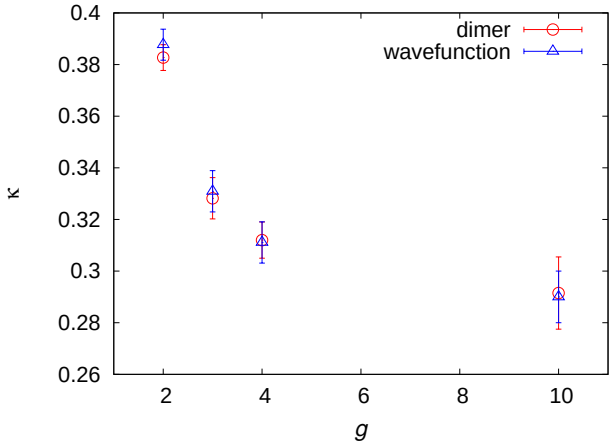

FIG. 14: Comparisons of the estimated values of κ_w and κ_d, obtained from our wavefunction and dimer model studies for $g = 2, 3, 4, 10$. Our consolidated estimates, considering all three ways of extracting κ on an equal footing, are as follows: $\kappa_d(2) = 0.383(5)$, $\kappa_w(2) = 0.388(6)$, $\kappa_d(3) = 0.328(8)$, $\kappa_w(3) = 0.331(8)$, $\kappa_d(4) = 0.312(7)$, $\kappa_w(4) = 0.311(8)$, $\kappa_d(10) = 0.292(14)$, and $\kappa_w(10) = 0.290(10)$. Error bars in these consolidated estimates reflect the spread between three different ways of estimating κ_w and κ_d, as well as statistical errors in the individual estimates.

$\mathcal{B}_g = 9g^4/(16(g^2-1)^2)$ is a normalization introduced to ensure that the *leading contribution* to the estimator[13–16] for this correlation function is independent of the value of g (this leading contribution comes from loop configurations in which $\vec{r}$ and its neighbour both lie in one loop, and $\vec{r}+\vec{R}$ and its neighbour both lie in another loop). If the correlator of $V_{\vec{r}}$ decays as $1/r^{\eta_w(g)}$, we expect this to be reflected in a $1/L^{\eta_w(g)}$ decay of $D(\vec{R}_{\alpha L})$ for fixed α.

Fig. 5 displays the exponential decay of the spin-correlation function, with correlation length of order half the spacing between two consecutive A sublattice sites. In sharp contrast to this behaviour, we find that the correlator of $V_{\vec{r}}$ decays as a slow power-law $\sim r^{-\eta_w(g)}$ where $\eta_w(g)$ is an increasing function of g. This is clear from Fig. 6, which shows the L dependence of $D(\vec{R}_{\alpha L})$ for $\alpha = 1/6$. As noted earlier, we may extract an effective stiffness $\kappa_w(g)$ from this power-law exponent $\eta_w(g)$ via the relation $\kappa_w(g) = 1/(\eta_w(g)\sqrt{3})$. In Fig. 7, we show the $|\vec{q}|$ dependence of $N(|\vec{q}|)$, the average valence-bond correlator defined earlier in Sec. III (averaged over six quantities, all of which are expected to tend to the limit $1/(4\pi\kappa_w)$ in the small $|\vec{q}|$ limit) and measured in the zero-winding sector. From this limiting behaviour of $N(|\vec{q}|)$, we are able to extract our most accurate estimate of $\kappa_w(g)$. Finally, we display winding sector probabilities (in the restricted ensemble in which both bra and ket valence bonds have the same winding numbers) from our wavefunction simulations in Fig. 8. By fitting these to an exponentially decaying function of $w^2 \equiv w_x^2 + w_y^2 + w_z^2$, we obtain a third independent estimate of $\kappa_w(g)$.

In order to test the correspondence between bond-energy correlations in the SU(g) wavefunction and dimer correlations in the interacting dimer model, we characterize VBS order in the interacting dimer model in a completely analogous way, in terms of the columnar VBS order parameter $\Psi_d = \sum_{\vec{r}} V_{\vec{r}}^{(d)}$, where $V_{\vec{r}}^{(d)}$ is the local VBS order parameter field defined as:

$$V_{\vec{r}}^{(d)} = (n_0(\vec{r}) + e^{2\pi i/3} n_1(\vec{r}) + e^{4\pi i/3} n_2(\vec{r}))e^{i\vec{Q}\cdot\vec{r}}\,. \quad (29)$$

Here $n_\mu(\vec{r})$ ($\mu = 0, 1, 2$) denotes the dimer occupation number on the bond labeled by μ and $\vec{r}$ (Fig. 3), and $\mathbf{Q} \equiv (2\pi/3, -2\pi/3)$ (Fig. 3).

To probe the VBS order in the system, we compute correlations of $V_{\vec{r}}^{(d)}$

$$D^{(d)}(\vec{R}_{\alpha L}) = \frac{1}{L^2}\sum_{\vec{r}} \langle (V_{\vec{r}+\vec{R}}^{(d)})^\dagger V_{\vec{r}}^{(d)} + (V_{\vec{r}}^{(d)})^\dagger V_{\vec{r}+\vec{R}}^{(d)} \rangle \quad (30)$$

at separations $\vec{R}_{\alpha L} = (\alpha L, \alpha L)$ with $\alpha = \frac{1}{3}, \frac{1}{4}, \frac{1}{6}$. As in the wavefunction case, we expect D^d to decay as $1/L^{\eta_d(g)}$ when correlations of $V_{\vec{r}}^d$ decay as $1/r^{\eta_d(g)}$. In Fig. 9, we see that this is indeed the case. From power-law fits to this behaviour, we obtain $\eta_d(g)$, and thence, an estimate for $\kappa_d(g) = 1/(\eta_d(g)\sqrt{3})$. In Fig. 11, we show our data in the zero-winding sector for the average $N(|\vec{q}|)$ of the six dimer correlators that are all expected to approach $1/(4\pi\kappa_d)$ in the limit of small $|\vec{q}|$ (as discussed in Sec. III). From the limiting behaviour of this function, we obtain a very accurate estimate for $\kappa_d(g)$. Finally, we display the relative probabilities for different winding sectors in Fig. 11. Fitting this to an exponentially decaying function of $w^2 \equiv w_x^2 + w_y^2 + w_z^2$ gives us a third independent estimate of $\kappa_d(g)$.

Fig. 12 and Fig. 13 show the values obtained for $\kappa_d(g)$ and $\kappa_w(g)$ in these three ways. As is clear from these figures, all three ways of extracting a stiffness are in rather good mutual agreement both for the wavefunction, and for the interacting dimer model. This is strong

evidence for the correctness of the coarse-grained height-description in both cases. Finally, in Fig. 14, we display the average of the three estimates for $\kappa_w(g)$ compared with the corresponding average of estimates for $\kappa_d(g)$. As is clear from this figure, the interacting dimer models studied at each g provide a remarkably good quantitative account of the long-distance properties of the SU(g) wavefunction. This is our main result.

VI. DISCUSSION

Does this correspondence with an interacting dimer model continue to provide useful insights when the RVB wavefunction has longer-range bipartite valence bonds while preserving the Marshal sign-structure[28] on the honeycomb lattice? The answer is clearly yes, although the form of the interactions gets correspondingly more complicated. What about more complicated wavefunctions which also have a non-trivial sign-structure (in the S^z basis), as is expected to be the case in the ground-state[29,30] of the honeycomb-lattice Heisenberg model with frustrating further neighbour couplings? The answer is much less clear since the non-trivial sign structure would necessarily lead to a description with Boltzmann weights carrying non-trivial phase-factors when expressed in the valence-bond basis. In this context, it is perhaps useful to note that certain dimer models with such general Boltzmann weights have recently been solved on the square lattice[31]. In another recent strand of work[32,33], it has also been shown that a class of nnRVB wavefunctions on frustrated planar lattices can be rewritten in the S^z basis as a sign-free partition sum with "Boltzmann weights" expressed in terms of Pfaffians, thereby allowing efficient Monte-Carlo calculation of physical observables. It would be interesting to ask if these Boltzmann weights have a controlled expansion in terms of some classical spin model with tractable interactions. What about the three-dimensional case? In the isotropic case[10], the framework used here is of very limited utility since overlap loops are long and the nnRVB wavefunction has Néel order. However, the present framework should be able to provide some insights into the nature of the spin-liquid phases explored recently in anisotropic three-dimensional RVB wavefunctions[11].

VII. ACKNOWLEDGEMENTS

One of us (KD) would like to thank F. Alet for useful discussions about the results of Ref. 5. This project was initiated under the umbrella of the Gulmohar Center (IIT Bombay), while the final stages of this project were supported by the Visiting Student Research Program of the TIFR. The authors are grateful to both institutions for making this collaboration possible. This research was supported by the Indo-French Centre for the Promotion of Advanced Research (IFCPAR/CEFIPRA) under Project 4504-1, and used computational resources funded by DST-SR/S2/RJN-25/2006 in addition to departmental computational resources of the Dept. of Theoretical Physics of the TIFR.

[1] P. Fazekas and P. W. Anderson, Philosophical Magazine 30, 423-440 (1974).
[2] W. Marshall, Proc. R. Soc. London, Ser. A 232, 48 (1955)
[3] S. Liang, B. Doucot, and P. W. Anderson, Phys. Rev. Lett. 61, 365 (1988).
[4] Y. Tang, A. W. Sandvik, C. L. Henley, Phys. Rev. B **84**, 174427 (2011).
[5] A. F. Albuquerque, F. Alet, Phys. Rev. B **82**, 180408(R) (2010).
[6] A. W. Sandvik, and H. G. Evertz, Phys. Rev. B **82**, 024407 (2010).
[7] J. Cano and P. Fendley, Phys. Rev. Lett. **105**, 067205 (2010).
[8] K. Damle, D. Dhar, K. Ramola, Phys. Rev. Lett. **108**, 247216 (2012).
[9] J.-M. Stéphan, H. Ju, P. Fendley, and R. G. Melko, New. J. Phys. **15**, 015004 (2013).
[10] A. F. Albuquerque, F. Alet, and R. Moessner, Phys. Rev. Lett. **109**, 147204 (2012).
[11] J. Xu and K. S. D. Beach, arXiv:1311.0004 (unpublished).
[12] K. Damle, unpublished.
[13] B. Sutherland, Phys. Rev. B **37**, 3786(R) (1988).
[14] K. S. D. Beach and A. W. Sandvik, Nuclear Physics B **750**, 142 (2006).
[15] K. S. D. Beach, F. Alet, M. Mambrini, S. Capponi, Phys. Rev. B 80, 184401 (2009).
[16] J. Lou, A. W. Sandvik, and N. Kawashima, Phys. Rev. B **80**, 180414(R) (2009).
[17] R. Youngblood, J. D. Axe, and B. M. McCoy, Phys. Rev. B **21**, 5212 (1980).
[18] R. Youngblood and J. D. Axe, Phys. Rev. B **23**, 232 (1981).
[19] H. W. J. Blote and H. J. Hillhorst, J. Phys. A **15**, L631 (1982).
[20] B. Nienhuis, H. W. J. Blote, and H. J. Hillhorst, J. Phys. A **17**, 3559 (1984).
[21] J. Kondev and C. L. Henley, Phys. Rev. B **52**, 6628 (1995); Nucl. Phys. B **464**, 540 (1996).
[22] C. Zeng and C. L. Henley, Phys. Rev. B **55**, 14935 (1997).
[23] R. Raghavan, C. L. Henley, and S. L. Arouh, J. Stat. Phys. **86**, 517 (1997).
[24] E. Fradkin, D. A. Huse, R. Moessner, V. Oganesyan, and S. L. Sondhi, Phys. Rev. B **69**, 224415 (2004).
[25] R. Kenyon, Comm. Math. Phys. **281**, 675 (2008).
[26] C. Boutillier and B. de Tiliére, Ann. of Prob. **37**, 1747 (2009).
[27] F. Alet *et. al.*, Phys. Rev. E **74**, 041124 (2006).
[28] Z. Nourbakhsh, F. Shahbazi, S. A. Jafari, and G. Baskaran, J. Phys. Soc. Jpn. **78**, 054701 (2009).
[29] H. Mosadeq, F. Shahbazi, S. A. Jafari, J. Phys.: Condens. Matter **23**, 226006 (2011).

[30] A. F. Albuquerque, D. Schwandt, B. Hetényi, S. Capponi, M. Mambrini, A. M. Lauchli, Phys. Rev. B **84**, 024406 (2011).
[31] A. Aiyyer, arXiv:1311.5965v1 (unpublished).
[32] J. Wildeboer and A. Seidel, Phys. Rev. Lett. **109**, 147208 (2012).
[33] F. Yang and H. Yao, Phys. Rev. Lett. **109**, 147209 (2012).